Anisotropy of a Selective Laser-Melted Ti–6Al–4V Lattice Structure

Dingye YAO
Shanghai University of Engineering Science
Weixing ZHOU
Shanghai Sanyou Medical Co., Ltd
Yuli MA
Shanghai Sanyou Medical Co., Ltd
Bo He (hebo@sues.edu.cn)
Shanghai University of Engineering Science

Research Article

Keywords: Selective laser melting, Lattice structure, Size effect, Anisotropy, Numerical simulation

Posted Date: November 8th, 2021

DOI: https://doi.org/10.21203/rs.3.rs-1018975/v1

Anisotropy of a selective laser-melted Ti–6Al–4V lattice structure

YAO Dingye[a, b], ZHOU Weixing[c], MA Yuli[c], HE Bo[a, b, *]

[a] School of Materials Engineering, Shanghai University of Engineering Science, Shanghai, China

[b] Research Center of High-temperature Alloy Precision Forming, Shanghai University of Engineering Science, Shanghai, China

[c] Shanghai Sanyou Medical Co., Ltd, Shanghai, China

[*] Corresponding Author, Email: hebo@sues.edu.cn

Abstract

Selective laser melting (SLM) is a widely adopted additive manufacturing process for the preparation of metallic lattice structures. However, it causes a build-direction-dependent anisotropy of morphologies, microstructures, and mechanical properties, making it difficult to predict the behavior and performance of lattice structures. In this study, tensile samples with different cross-sections and build directions (BDs) were fabricated by SLM. The anisotropic morphology, microstructure, and tensile properties were observed and measured using optical microscopy, scanning electron microscopy, and three-dimensional digital image correlation to determine the effects of the size and BD of SLMed materials. The extracted data were sequentially used to modify the geometric and physical models of the lattice. Body-centered cubic lattice structures were fabricated by SLM, and compression tests were performed to verify the modified compression model. In addition to the BD-related grains, the cross-sectional area of the SLMed sample affects its mechanical properties. The small cross-section makes the microstructure finer because the proportion of the contour path that uses higher power is no longer negligible. The sample with small cross-section has more anisotropy because of the lack of tolerance to heterogeneity and macro defects like roughness. In this study, by analyzing samples with small cross-sections, a model consisting of an isotropic hardening law and Hill's anisotropic yield function is established to describe the yield and plasticity behavior of the as-built SLMed Ti–6Al–4V lattice. The simulated and experimental data fit very well, verifying the methodology employed in this study.

Key words

Selective laser melting, Lattice structure, Size effect, Anisotropy, Numerical simulation

1. Introduction

Periodic metallic lattice structures are gaining popularity in the aerospace and medical industries owing to their high stiffness-to-weight ratios and design freedom. Because of the advantages in the preparation of complex features, additive manufacturing (AM) based on powder bed fusion is widely adopted as a method for preparing lattice structures [1-5]. As AM is a novel preparation method developed in the recent decades, it is yet to be used in key applications, particularly in the long term under varied loading owing to the severe lack of property and

performance data. Simulation is a rapid and energy-conserving path for achieving abundant data by predicting the performance of an AMed part, provided the property metadata used in the physical model are correctly measured in the experiment.

However, the anisotropy of the AMed alloy is always significant and unpredictable. The main reason for this is the extreme conditions of the AM. A high cooling rate (10^3–10^8 K/s) and a large temperature gradient, which are higher than those of the other preparation methods, leads to inhomogeneous microstructures [6-13]. In the case of Ti–6Al–4V alloy, the consequent epitaxial growth of prior-β under such extreme thermal conditions results in the excessive formation of large-size, columnar, and build-direction-paralleled grains [14-17]. As a result, the strength of the AMed-alloy in the direction perpendicular to the building direction (BD) is always 2–30% greater than that along the BD, and cracks preferentially form along the periphery of these through-thickness grains [7, 18].

In addition to the thermal conditions, both sample and local feature size of the AMed part also play an essential role in the microstructure and the consequent mechanical properties. It was reported that the thickness of the α'-lath, the size of the prior-β grain of AMed Ti–6Al–4V, and its strength and ductility depend on the sample size [19].

Using the mechanical properties obtained from bulk AMed materials as the metadata of the simulation may cause a mismatch. Moreover, the lattice can be either bending- or stretching-dominated [20] depending on the loading mode. This means that the true stress state in the lattice structure could be intricate and polydirectional, and a mechanical model of the lattice should be calculated more accurately.

In this study, the morphology, microstructure, and compression performance of body centered cubic (BCC) lattice structures of selective-laser-melted (SLM) Ti–6Al–4V were observed and quantitatively measured, and the effect of sample size on the microstructure and tensile properties was determined. Tensile samples with different build orientations were examined. The orientation-dependent mechanical properties were extracted from the tensile tests of small cross-sectional Ti–6Al–4V. The plastic behavior of the SLMed small cross-sectional Ti–6Al–4V samples was quantitatively characterized using a digital image technique and was formulated using Hill's anisotropic yield function [21, 22]. The corrected computer-aided design (CAD) models and a constitutive model were applied to a finite element (FE) model of uniaxial compression of the BCC lattice structure and sequentially validated by experiments.

2. Materials and methods

2.1 Sample design and preparation

All the samples were fabricated by SLM on an EOS EOSINT M290 AM system. The chemical composition of Ti–6Al–4V is presented in Table 1. During scanning, for each layer, the profile was first scanned and the area within the profile was melted subsequently. The processing parameters are presented in Table 2.

Table 1
Chemical composition (at.%) of Ti-6Al-4V powder.

Ti	Al	V	O	N	H	Fe	C	Y	Other Elements

Bal.	6.44	4.15	0.07	<0.01	0.001	0.19	<0.01	<0.005	<0.40

Table 2
SLM printing parameters.

Laser power (P) (contour/ hatch) [W]	Scanning speed (v) [mm/s]	Hatch spacing (h) [μm]	Layer thickness (d) [μm]	Scan rotation [°]
280/180	1000	150	30	67

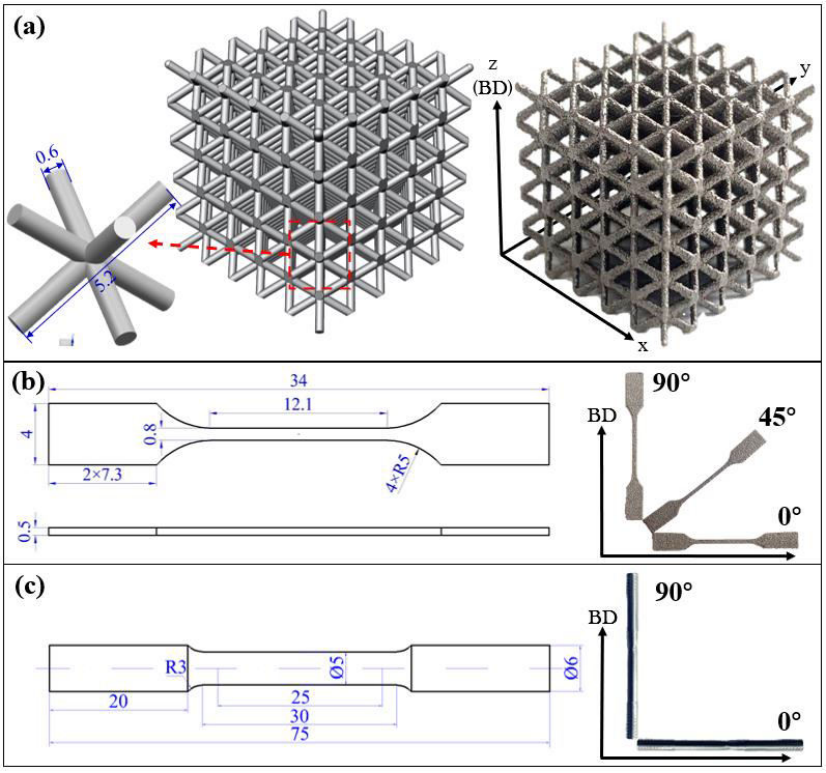

Fig.1 (a) BCC lattice structure, designed and as-printed;
(b) small cross-sectional tensile specimen and (c) large cross-sectional tensile specimen, and their preparation positions (angles) vs build orientations. Dimension unit is millimeter

A 5×5×5 unit BCC lattice structure was chosen for this investigation, as illustrated in Fig. 1a. The length (L) and diameter (D) of each strut was 5.2 and 0.6 mm, respectively. After printing, the lattices were ultrasonically cleaned to remove the loose adhesive powder. Both ends of the lattice structure were polished to remove the support as well as to lower the lateral friction that could lead to the barreling of the sample during the compression test.

Small cross-sectional tensile specimens (Fig. 1b) prepared with different angles vs. the BD are denoted as the H-sample (horizontal sample, perpendicular to the BD), I-sample (45° angle inclined sample vs. the BD), and V-sample (vertical sample, parallel to the BD). Five samples were fabricated in each angle. A rectangular cross-section was chosen for measuring the reduction in width and thickness during tension. To emphasize the size effect, the cross-section was designed to be as small as 0.4 mm^2, physically simulating the dimension and thermal history of the lattice structure. Tensile specimens with a larger cross-section of 19.6 mm^2 were prepared in two angles of 0° and 90°, with five samples each (Fig. 1c). Both types of tensile specimens were polished before

testing to reduce the surface roughness. The number of each kind of tensile specimen is listed below.

Table 3
The number of each kind of tensile specimen.

		Building direction		
		0°	45°	90°
Cross-sectional area	0.4mm^2	5	5	5
	19.6mm^2	5	-	5

2.2 Characterization and testing

Samples were ground, polished, and etched using Kroll's reagent (2% HF, 6% HNO_3, and 93% water). The morphologies and microstructures were characterized using a digital optical microscope (SDPTOP ICX41M).

To determine the uniaxial compressive properties of these lattice structures, quasi-static uniaxial compression tests were performed using a WDW-100 electronic universal testing machine equipped with a 100-kN force cell. A constant displacement rate of 1 mm/min was selected according to the ISO 13314 standard. To determine the orientation effect on the compression properties of the SLMed BCC lattice structure, six samples were divided into two groups and compressed under a load parallel or perpendicular to the BD. The compression tests were terminated at 40% compressive engineering strain. The compressive stress (σ) was calculated by dividing the compression force by the original contour area of 225 mm^2, and the strain (ε) was calculated by dividing the load cell displacement by lattice structure height (15 mm). The entire compression process was recorded by a digital camera to capture the collapse behavior of the lattice at different strain states.

Quasi-static uniaxial tensile testing of large cross-sectional samples was carried out using a SUNS CMT5105 testing machine equipped with a 100 kN force cell, with a displacement rate of 1 mm/min. Quasi-static uniaxial tensile testing of the small cross-sectional tensile specimens was conducted using a Shimadzu AGS-X testing machine equipped with a 5 kN capacity load cell, with a displacement rate of 1 mm/min. All tensile tests were carried out after grinding the surface of the sample to eliminate the influence of roughness. Non-contact full-field displacement measurements were conducted using an XTOP 3D digital image correlation (DIC) system.

The plastic strain ratio (r) was calculated from the captured true plastic width strain (ε_{pb}) and true plastic thickness strain (ε_{pa}) using Equation (1).

$$r = \frac{\varepsilon_{pb}}{\varepsilon_{pa}} \tag{1}$$

2.3 Numerical simulation

The FE model for the simulation of uniaxial compression on the lattice structure was established using ABAQUS®. Relevant elastic mechanical properties, such as the Young's modulus and Poisson's ratio, were obtained from the tensile experiments of the small cross-sectional samples.

A solid linear tetrahedral element C3D8 was used. Both the compressive plate and baseplate were simplified and simulated with discrete rigid plates and meshed using rigid bilinear quadrilateral elements (R3D4). A surface-to-surface contact with a 'penalty' friction was defined between the lattice structure and the rigid plates in the tangential direction, and the friction coefficient was set as 0.1 based on the experimental data. A 'hard' type relationship is selected for the contact in the normal direction. A displacement load that terminates at 20% compressive strain, with a smooth step amplitude, was applied to the reference point of the rigid compressive plate. All the rotational and translational degrees of freedom of the rigid baseplate were constrained at the reference point in an 'encastre' state. Rigid body movements were removed by constraining the symmetry axis at the top and bottom planes of the FE models.

3. Results and discussion

3.1 Microstructure and properties

The morphology of the struts is shown in Fig. 2. It can be observed in Fig. 2a that because of the staircase effect [23], the cross-section of the strut is elliptical with a short axis (0.59 mm) and a long axis (0.63 mm). Fig. 2b and 2c demonstrate the morphology of the strut projected on $(1\ 1\ 2)$ and $(1\ \bar{1}\ 0)$ planes of the lattice, respectively; the latter is rougher and thicker with some small particles (red dotted line in Fig. 2c) attached to the lower side.

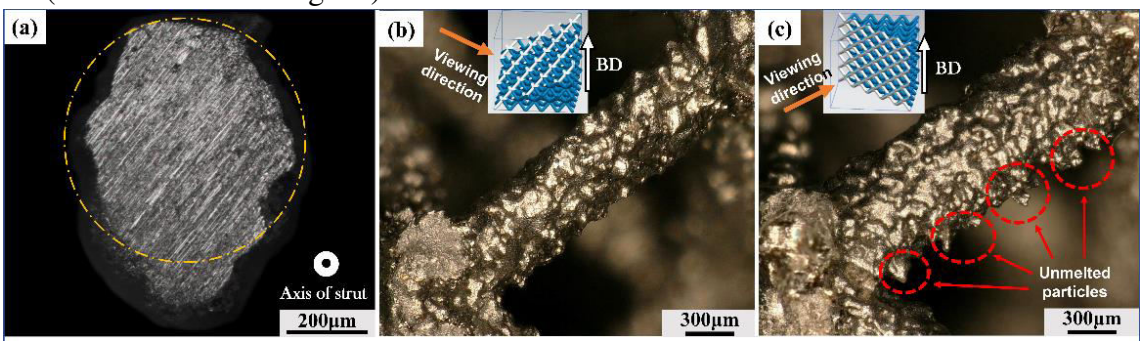

Fig. 2 The morphologies of struts on different surfaces (a) cross section; (b) $(1\ 1\ 2)$ projection plane; (c) $(1\ \bar{1}\ 0)$ projection plane

The microstructure of the as-built lattice structure is also directly related (Fig. 3), and the through-thickness prior-β grains exist in the strut (Fig. 3a) and node (Fig. 3b). These columnar grains are several hundred microns high and a few tens of microns wide.

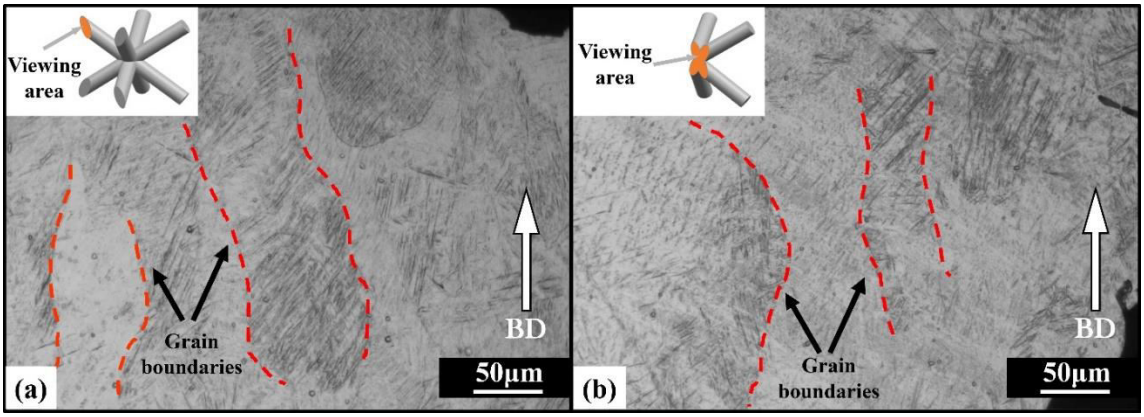

Fig. 3 The microstructure of as-built Ti-6Al-4V lattice structure

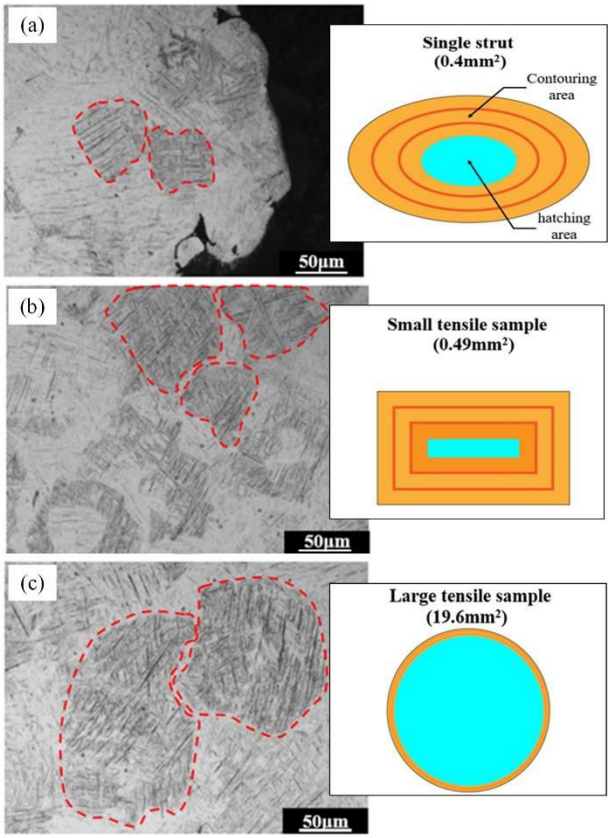

Fig. 4 Dimensions of prior-β grain in (a) lattice struts, (b) small cross-section tensile sample, (c) large cross-section tensile sample, and the proportion of their contour path to the cross section

The microstructures of the struts and the two types of tensile samples are compared in Fig. 4. The size of the columnar prior-β grains of the small cross-sectional tensile samples (Fig. 4b) is approximately 50 μm and is close to that of the struts (Fig. 4a). However, the prior-β grain of the large cross-sectional tensile sample (Fig. 4c) is far larger, with a dimension of hundreds of microns. This phenomenon may be the result of the contour scanning of the samples used in this study. As the size of the cross-sectional area decreases, the proportion of the contour path in the total cross-sectional area increases as illustrated in Fig. 4. When the area was designed to be sufficiently small at approximately 0.4 mm^2, similar to the struts and small cross-sectional tensile samples in this study, the area of the contour path accounted for more than 85% of the total cross-section, and the difference between the contour laser power (280 W) and the hatch laser power (180 W) could longer be neglected. The laser energy density (LED) [24] ($LED = P/(v \cdot h \cdot d)$) increased with laser power, and the microstructure determined by the LED changed. The higher temperature gradient from the boosted LED, together with the higher solidification rate due to the high surface-to-volume ratio, caused the microstructure to evolve from coarse to fine as the sample dimensions decreased.

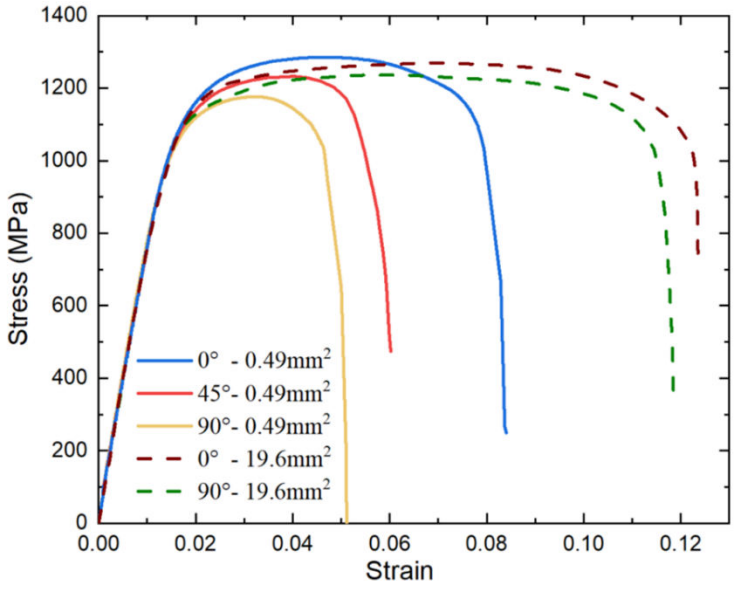

Fig. 5 Stress-strain curves for SLMed Ti-6Al-4V tensile samples with different size of cross section and different orientation

Table 4
Tensile properties for SLMed Ti-6Al-4V specimens with different angles and cross-sectional areas.

	0.49mm^2			19.6mm^2	
	H-sample	I-sample	V-sample	H-sample	V-sample
Yield strength (MPa)	1108.7	1084.7	1046.8	1133.8	1096.2
Ultimate tensile strength (MPa)	1285.1	1243.1	1176.0	1271.3	1231.2
Elongation (%)	7.5	5.2	4.3	10.4	9.5
Anisotropy in yield strength (%)	5.6			3.3	
Anisotropy in ultimate tensile strength (%)	8.5			3.2	
Anisotropy in elongation (%)	42.7			8.7	

The stress–strain analysis of the two types of tensile specimens with different cross-sectional areas are presented in Fig. 5 and Table 4. We defined the anisotropy as $\frac{\sigma_H - \sigma_V}{\sigma_H} \times 100\%$ [25], where σ_H and σ_V denoted the mechanical properties in the H-sample and V-sample, respectively. The H-samples, either large or small, had higher strengths and elongations than the V-samples. A similar tendency was found in 18Ni (300)-grade maraging steel [21] and 316L [26] prepared by SLM, suggesting that the defects formed among the layers played a major role in the simultaneous decrease of strength and ductility. Meanwhile, compared to large cross-sectional samples, the anisotropy of small cross-sectional samples was more significant, indicating that the small cross-sections were more sensitive to heterogeneity and macro defects.

3.2 Lattice compression

The compression behavior of the as-built sample was investigated in both parallel and perpendicular directions to BD, and two typical curves (Fig. 6) with obvious differences indicated that the lattice was anisotropic because, due to symmetry, a 5 × 5 × 5 unit BCC lattice structure should have shown the same curves regardless of the direction relative to the BD. Table 5 shows the data extracted from the curves.

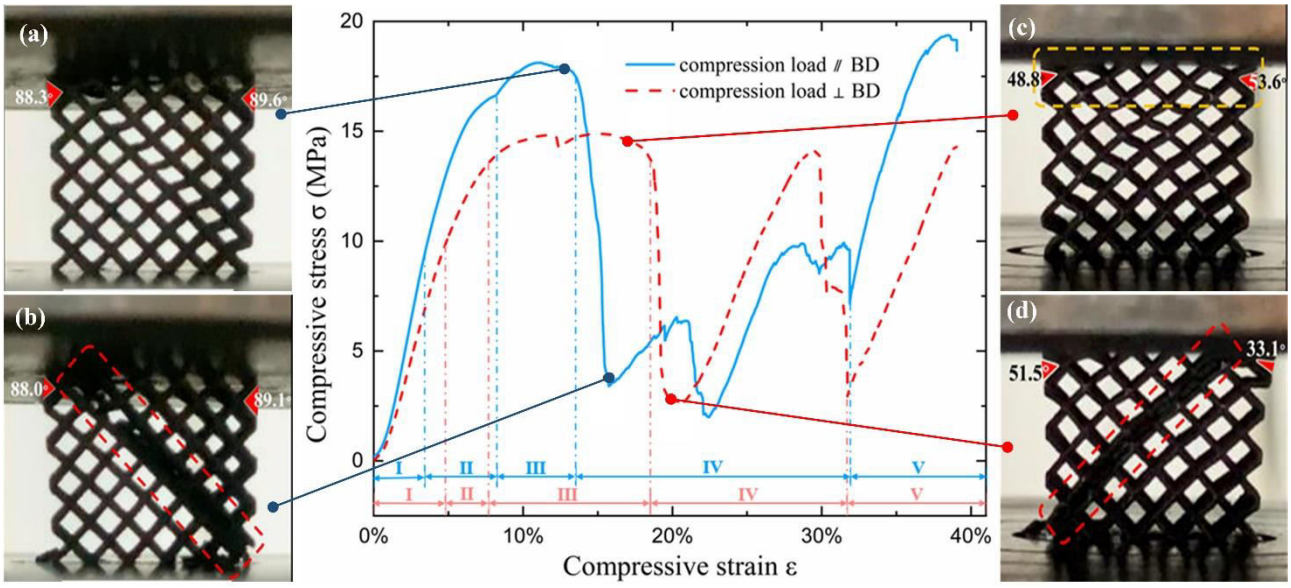

Fig. 6 Quasi-static uniaxial compressive stress-strain curves of SLMed BCC lattice structures along different compression axes. (a, c) The crack bands initialized and (b, d) the crack bands closed

Table 5
Compressive properties of BCC lattice structure along different axes.

	// BD	**⊥ BD**
Elastic modulus [MPa]	348.8	248.3
compressive strength [MPa]	18.0	14.6
Energy absorption (30% strain) [MJ/m^3]	2.9	3.2
Strain at maximum stress(%)	11.2	15.9

The two curves showed five typical stages, according to the tendency. Stage I was relatively linear with a very short curved beginning. The linear part of this stage represented the elastic behavior of the lattice structure, and the slope was the elastic modulus of the lattice. The curved portion of stage I from 0 to ~1%, however, resulted from an accumulation term that occurred before all the struts were completely contacted during compression. This portion was ignored in this study because of its shorter length. Elastic modulus of the compression parallel to the BD is 40.5% higher than that of the compression perpendicular to BD because the shape of the cross-section has changed from circular to elliptical, with the long axis nearly parallel to the load. This increases the moment of inertia of the struts and make them capable of resisting the bending induced by the compression.

Once the elastic limit was reached, plastic deformation started as struts began to yield, and the

curves entered stage II. The modulus started to decrease, but the strength increased until stage III, where the stress increased to the first peak. The lattice compressed parallel to the BD stayed at the peak for a shorter time, whereas that compressed perpendicular to the BD stayed longer, although the value of the peak stress was lower. Subsequently, both curves decreased rapidly, and the parallel and perpendicular lattices showcased a sharp descent at approximately 13% and 19% strain, respectively. The stress of both samples dropped by approximately 80% after the first peak stress, which was larger than the 56% reported in the literature [27] for a heat-treated Ti–6Al4–V lattice, indicating its ductility. As we consider the area under the stress–strain curve as the energy absorption capability [28], we found that the lattice compressed parallel to the BD has a higher peak strength, whereas the one compressed perpendicular to the BD had a better energy absorption ability of 11.5%. As the compression continued, the struts deformed so severely that contact with others sometimes formed a fluctuant stage IV, until finally losing all the capability of compression to form the final stage V.

The two compression directions had different modes, as shown in Fig. 6. When the compression load was parallel to the BD, the lattice structures deformed uniformly up to 12% strain, and then a diagonal crack band initialized at 45° to the loading direction (Fig. 6a). This holistic destruction was catastrophic to the bearing capacity of the lattice structure, causing a steep stress drop. The crack band (emphasized by the red dotted line in Fig. 6b) finally closed at a strain of 15.4%, which corresponded to the first valley of the stress–strain curve. The variation in the angles of the struts in the first layer was small, within two degrees.

In contrast, when the compression load was perpendicular to the BD, the diagonal crack band initialized much later (strain of 16.1%). At that time, the angles between the struts in the first layer were reduced by more than 40% compared to that of the initial state (emphasized by the yellow dotted line in Fig. 6c). This suggested that the first layer which contacted the compressive plate was crushed before the diagonal crack band was initialized. This local failure reduced the bearing capacity of the entire structure, resulting in a smaller compressive strength and postponing the holistic destruction. This different failure mode consequently enlarged the area under the stress curve, implying a higher capacity for energy absorption.

3.3 Numerical simulation

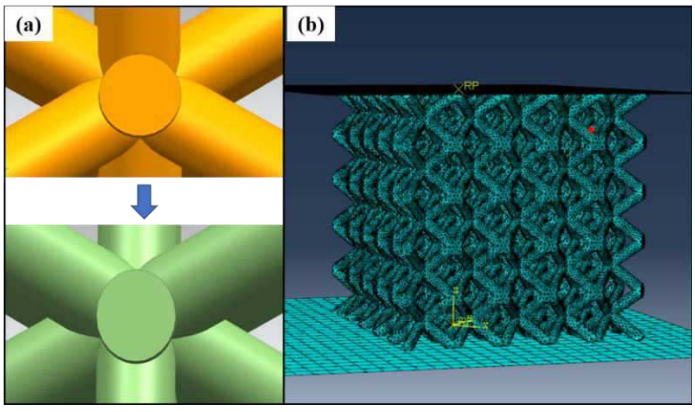

Fig. 7 (a) The CAD model modification and (b) FE model

Based on the above discussion, it was necessary to modify the model both in geometrically and

physically. First, the cross-section of the struts was modeled as an ellipse with a 0.72 mm long axis and 0.58 mm short axis, as shown in Fig. 7a. Then, Hill's function was adopted to establish an anisotropic yield criterion using the data extracted from the DIC of small cross-sectional samples.

Hill's anisotropic function can be expressed in terms of rectangular Cartesian stress components as follows:

$$\sigma_{Hill} = \sqrt{F(\sigma_{22}-\sigma_{33})^2 + G(\sigma_{33}-\sigma_{11})^2 + H(\sigma_{11}-\sigma_{22})^2 + 2L\sigma_{23}^2 + 2M\sigma_{31}^2 + 2N\sigma_{12}^2} \quad (2)$$

where σ_{ij} is the stress component and F, G, H, L, M, and N are the Hill's constants obtained by tests of the material in different orientations, which are defined as:

$$F = \frac{(\sigma^0)^2}{2}\left(\frac{1}{\bar{\sigma}_{22}^2} + \frac{1}{\bar{\sigma}_{33}^2} - \frac{1}{\bar{\sigma}_{11}^2}\right),$$

$$G = \frac{(\sigma^0)^2}{2}\left(\frac{1}{\bar{\sigma}_{33}^2} + \frac{1}{\bar{\sigma}_{11}^2} - \frac{1}{\bar{\sigma}_{22}^2}\right),$$

$$H = \frac{(\sigma^0)^2}{2}\left(\frac{1}{\bar{\sigma}_{11}^2} + \frac{1}{\bar{\sigma}_{22}^2} - \frac{1}{\bar{\sigma}_{33}^2}\right),$$

$$L = \frac{3}{2}\left(\frac{\tau^0}{\bar{\sigma}_{23}}\right)^2,$$

$$M = \frac{3}{2}\left(\frac{\tau^0}{\bar{\sigma}_{13}}\right)^2,$$

$$N = \frac{3}{2}\left(\frac{\tau^0}{\bar{\sigma}_{12}}\right)^2, \quad (3)$$

where $\bar{\sigma}_{ij}$ is the yield stress: when $i = j$, it represents the tensile yield stresses, when $i \neq j$, it represents the shear yield stress; σ^0 is the reference tensile yield stress, which was taken from the yield stress of 0° samples, τ^0 is the reference shear yield stress, and $\tau^0 = \sigma^0/\sqrt{3}$.

Eq. (3) can be rewritten as:

$$F = \frac{1}{2}\left(\frac{1}{R_{22}^2} + \frac{1}{R_{33}^2} - \frac{1}{R_{11}^2}\right),$$

$$G = \frac{1}{2}\left(\frac{1}{R_{33}^2} + \frac{1}{R_{11}^2} - \frac{1}{R_{22}^2}\right),$$

$$H = \frac{1}{2}\left(\frac{1}{R_{11}^2} + \frac{1}{R_{22}^2} - \frac{1}{R_{33}^2}\right),$$

$$L = \frac{3}{2R_{23}^2},$$

$$M = \frac{3}{2R_{13}^2},$$

$$N = \frac{3}{2R_{12}^2}, \quad (4)$$

Where R_{ij} are anisotropic yield stress ratios that are defined as follows:

$$R_{ij} = \begin{cases} \frac{\bar{\sigma}_{ij}}{\sigma^0}, when\ i = j \\ \frac{\bar{\sigma}_{ij}}{\tau^0}, when\ i \neq j \end{cases} \quad (5)$$

Using mathematical relationships, the strain ratios can be converted into stress ratios. Hill's constants can be formulated by the true plastic ratios (r), which are also known as Lankford's

coefficients:

$$R_{11} = \sqrt{\frac{r_{90}(r_0+1)}{(r_0+r_{90})}},\ R_{22} = 1,\ R_{33} = \sqrt{\frac{r_{90}(r_0+1)}{r_0(r_{90}+1)}},\ R_{23} = \sqrt{\frac{3(r_0+1)r_{90}}{(2r_{45}+1)(r_0+r_{90})}} \quad (6)$$

Based on the study of Bagherzadeh et al. [29] and Mooney et al. [21], it is reasonable to assume that $R_{12} = R_{31} = 1$. Using this definition, the anisotropic constitutive model of the as-built small cross-section was established, and the corresponding Hill's constants are listed in Table 6.

Table 6
Hill's constants for as-built small cross-sectional Ti-6Al-4V.

F	G	H	L	M	N
0.38	0.51	0.41	1.37	1.5	1.5

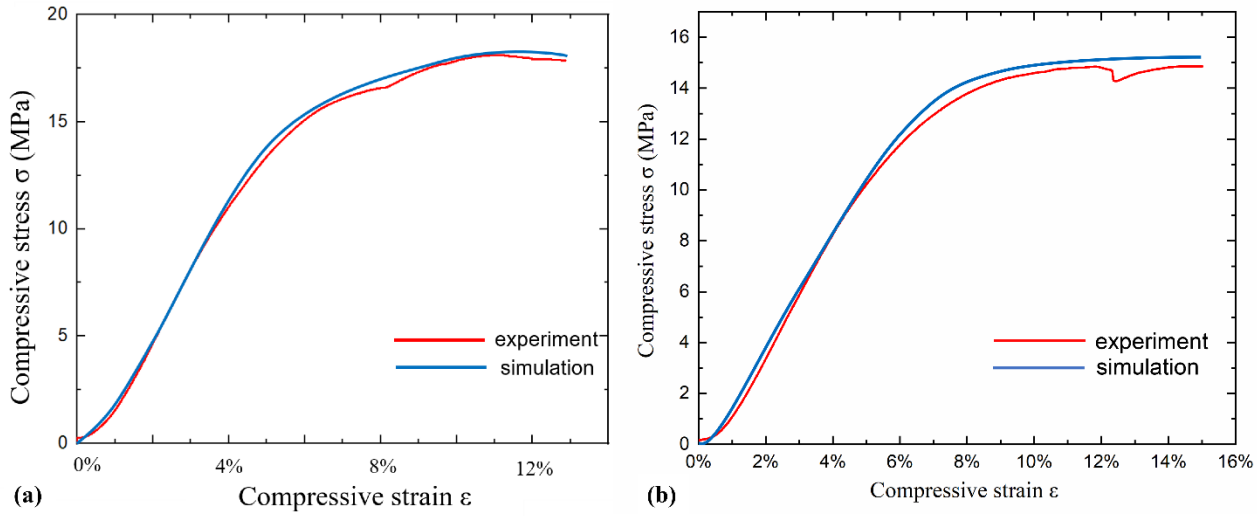

Fig. 8 Simulated and experimental stress-strain curves when compressed (a) parallel to BD, and (b) perpendicular to BD

Fig. 8 depicts the predicted and experimental stress–strain curves under different loading conditions. The simulated curve is good at predicting the compression and shows a perfect fit until a strain of 12%. The difference between the simulated and experimentally measured curves can be attributed to the absence of surface roughness in the CAD model. Some fluctuations observed in the experimental curve may be attributed to the undesired breakage of a few random struts. The simulation of compressing beyond 12% strain is not within the scope of this study and requires further investigation.

Conclusions

In this study, a series of Ti–6Al–4V BCC lattice and tensile specimens with different building directions and cross-sections were fabricated by SLM. The morphology, microstructure, and mechanical behavior of the specimens were examined. The processing-induced anisotropy was discussed, and a simulation model was constructed to predict the mechanical behavior of the lattice structure.

- The effect of the BD angle: The mechanical properties of the SLMed Ti–6Al–4V tensile

samples were measured as a function of the BD angle. As the BD angle decreased, the yield strength, ultimate tensile strength, and elongation increased monotonically because of the strongly textured prior-β grains parallel to the BD.

- The effect of cross-section: The size of the prior-β grain was positively associated with the sample size of the specimens owing to different thermal histories, such as the solidification rate and temperature gradient, and different ratios of the contour path, which lead to a non-negligible anisotropy, particularly in small cross-sectional samples. Furthermore, the unavoidable staircase effect led to an increase of one of the dimensions of the small cross-section sample by 22% compared to that of the original design, resulting in an increase in the anisotropy.
- Affected by the above anisotropies, the lattice structure showed an orientation-dependent compression performance and the elastic modulus, strength, energy absorption ability, and deformation behavior varied depending on the angles between the compression axis and the BD. This will be helpful for better design and use of lattice structures in engineering.
- In this study, by developing an accurate simulation model, we demonstrate a way to predict the mechanical properties of a lattice structure more precisely in the uniaxial compression tests.

Acknowledgements-+

The authors are grateful to XTOP 3D Technology (Shenzhen) Co., Ltd. for their support with the DIC measurements.

Declarations:

Funding: The authors did not receive support from any organization for the submitted work.
Conflict of Interest: The authors declare that they have no conflict of interest.
Availability of data and material: The data in this paper are obtained from experiments, and the simulated data is consistent with the experimental data. All data generated in this study are included in this manuscript.
Code availability: Not applicable.
Compliance with Ethical Standards: Not applicable.
Consent to participate: All authors have agreed to authorship, read and approved the manuscript, and given consent for submission and subsequent publication of the manuscript. The authors guarantee that the contribution to the work has not been previously published elsewhere.
Consent for publication: Publication has been approved by all co-authors and the responsible authorities at the institute(s) where the work has been carried out.
Authors' contributions: Yao Dingye: Participated in experimental design, experimental implementation, data collection, data analysis and paper writing; ZHOU Weixing: Participated in experimental implementation; MA Yuli: Participated in experimental implementation; HE Bo: Guided experimental design and data analysis, and critically reviewed the knowledge content of the article.

References

1. M Lowther, S Louth, A Davey, et al (2019) Clinical, industrial, and research perspectives on powder bed fusion additively manufactured metal implants. Addit Manuf, 28: 565-584. https://doi.org/10.1016/j.addma.2019.05.033
2. L E Murr (2020) Metallurgy principles applied to powder bed fusion 3D printing/additive manufacturing of personalized and optimized metal and alloy biomedical implants: an overview. J Mater Res Technol, 9: 1087-1103. https://doi.org/10.1016/j.jmrt.2019.12.015
3. T Maconachie, M Leary, B Lozanovski, et al (2019) SLM lattice structures: Properties, performance, applications and challenges. Mater Des, 183: https://doi.org/10.1016/j.matdes.2019.108137
4. C Omar Balderrama-Armendariz, E MacDonald, D Espalin, et al (2018) Torsion analysis of the anisotropic behavior of FDM technology. Int J Adv Manuf Technol, 96: 307-317. https://doi.org/10.1007/s00170-018-1602-0
5. C P Paul, S K Mishra, C H Premsingh, et al (2012) Studies on laser rapid manufacturing of cross-thin-walled porous structures of Inconel 625. Int J Adv Manuf Technol, 61: 757-770. https://doi.org/10.1007/s00170-011-3742-3
6. S Pauly, P Wang, U Kühn, et al (2018) Experimental determination of cooling rates in selectively laser-melted eutectic Al-33Cu. Addit Manuf, 22: 753-757. https://doi.org/10.1016/j.addma.2018.05.034
7. M Simonelli, Y Y Tse,C Tuck (2014) Effect of the build orientation on the mechanical properties and fracture modes of SLM Ti–6Al–4V. Mater Sci Eng A, 616: 1-11. https://doi.org/10.1016/j.msea.2014.07.086
8. V Cain, L Thijs, J Van Humbeeck, et al (2015) Crack propagation and fracture toughness of Ti6Al4V alloy produced by selective laser melting. Addit Manuf, 5: 68-76. https://doi.org/10.1016/j.addma.2014.12.006
9. C Qiu, N J E Adkins,M M Attallah (2013) Microstructure and tensile properties of selectively laser-melted and of HIPed laser-melted Ti–6Al–4V. Mater Sci Eng A, 578: 230-239. https://doi.org/10.1016/j.msea.2013.04.099
10. B Wysocki, P Maj, R Sitek, et al (2017) Laser and Electron Beam Additive Manufacturing Methods of Fabricating Titanium Bone Implants. Appl Sci, 7: https://doi.org/10.3390/app7070657
11. P Edwards, A O'Conner,M Ramulu (2013) Electron Beam Additive Manufacturing of Titanium Components: Properties and Performance. J Manuf Sci E, 135: https://doi.org/10.1115/1.4025773
12. H K Rafi, N V Karthik, H Gong, et al (2013) Microstructures and Mechanical Properties of Ti6Al4V Parts Fabricated by Selective Laser Melting and Electron Beam Melting. J Mater Eng Perform, 22: 3872-3883. https://doi.org/10.1007/s11665-013-0658-0
13. T Vilaro, C Colin, J D Bartout (2011) As-Fabricated and Heat-Treated Microstructures of the Ti-6Al-4V Alloy Processed by Selective Laser Melting.

Metall Mater Trans A, 42: 3190-3199. https://doi.org/10.1007/s11661-011-0731-y
14. A E Wilson-Heid, Z Wang, B McCornac, et al (2017) Quantitative relationship between anisotropic strain to failure and grain morphology in additively manufactured Ti-6Al-4V. Mater Sci Eng A, 706: 287-294. https://doi.org/10.1016/j.msea.2017.09.017
15. C J Todaro, M A Easton, D Qiu, et al (2020) Grain structure control during metal 3D printing by high-intensity ultrasound. Nat Commun, 11: 142. https://doi.org/10.1038/s41467-019-13874-z
16. P Wang, X Tan, M L S Nai, et al (2016) Spatial and geometrical-based characterization of microstructure and microhardness for an electron beam melted Ti–6Al–4V component. Mater Des, 95: 287-295. https://doi.org/10.1016/j.matdes.2016.01.093
17. X Tan, Y Kok, Y J Tan, et al (2015) Graded microstructure and mechanical properties of additive manufactured Ti–6Al–4V via electron beam melting. Acta Mater, 97: 1-16. https://doi.org/10.1016/j.actamat.2015.06.036
18. B E Carroll, T A Palmer,A M Beese (2015) Anisotropic tensile behavior of Ti–6Al–4V components fabricated with directed energy deposition additive manufacturing. Acta Materialia, 87: 309-320. https://doi.org/10.1016/j.actamat.2014.12.054
19. D Barba, C Alabort, Y T Tang, et al (2020) On the size and orientation effect in additive manufactured Ti-6Al-4V. Mater Des, 186: https://doi.org/10.1016/j.matdes.2019.108235
20. M F Ashby (2011) Chapter 11 - Designing Hybrid Materials. In: Materials Selection in Mechanical Design (Fourth Edition), M. F. Ashby, Editor. Butterworth-Heinemann: Oxford. pp. 299-340. https://doi.org/10.1016/B978-1-85617-663-7.00011-4
21. B Mooney, K I Kourousis, R Raghavendra, et al (2019) Process phenomena influencing the tensile and anisotropic characteristics of additively manufactured maraging steel. Mater Sci Eng A, 745: 115-125. https://doi.org/10.1016/j.msea.2018.12.070
22. A E Wilson-Heid, S Qin,A M Beese (2018) Anisotropic multiaxial plasticity model for laser powder bed fusion additively manufactured Ti-6Al-4V. Mater Sci Eng A, 738: 90-97. https://doi.org/10.1016/j.msea.2018.09.077
23. A Großmann, J Gosmann,C Mittelstedt (2019) Lightweight lattice structures in selective laser melting: Design, fabrication and mechanical properties. Mater Sci Eng A, 766: https://doi.org/10.1016/j.msea.2019.138356
24. D Herzog, V Seyda, E Wycisk, et al (2016) Additive manufacturing of metals. Acta Mater, 117: 371-392. https://doi.org/10.1016/j.actamat.2016.07.019
25. J Alcisto, A Enriquez, H Garcia, et al (2010) Tensile Properties and Microstructures of Laser-Formed Ti-6Al-4V. J Mater Eng Perform, 20: 203-212. https://doi.org/10.1007/s11665-010-9670-9
26. W Shifeng, L Shuai, W Qingsong, et al (2014) Effect of molten pool boundaries

on the mechanical properties of selective laser melting parts. J Mater Process Tech, 214: 2660-2667. https://doi.org/10.1016/j.jmatprotec.2014.06.002
27. N Jin, Z Yan, Y Wang, et al (2020) Effects of heat treatment on microstructure and mechanical properties of selective laser melted Ti-6Al-4V lattice materials. Int J Mech Sci: https://doi.org/10.1016/j.ijmecsci.2020.106042
28. D Guixin,W Shiping (2020) Research Progress of Light and Ultralight Porous Metal Materials (In Chinese). Foundry, 69: 1-10. https://kns.cnki.net/kcms/detail/detail.aspx?FileName=ZZZZ202001003&DbName=CJFQ2020
29. S Bagherzadeh, M J Mirnia,B Mollaei Dariani (2015) Numerical and experimental investigations of hydro-mechanical deep drawing process of laminated aluminum/steel sheets. J Manuf Process, 18: 131-140. https://doi.org/10.1016/j.jmapro.2015.03.004